White Rose Research Online
eprints@whiterose.ac.uk
https://eprints.whiterose.ac.uk
Universities of Leeds, Sheffield and York

Deposited via The University of Sheffield.

White Rose Research Online URL for this paper:
https://eprints.whiterose.ac.uk/id/eprint/102265/

Version: Accepted Version

Article:
McGrath, D.M., Ravikumar, N., Beltrachini, L. et al. (2017) Evaluation of Wave Delivery Methodology for Brain MRE: Insights from Computational Simulations. Magnetic Resonance in Medicine, 78 (1). pp. 341-356. ISSN: 0740-3194

https://doi.org/10.1002/mrm.26333

This is the peer reviewed version of the following article: McGrath, D. M., Ravikumar, N., Beltrachini, L., Wilkinson, I. D., Frangi, A. F. and Taylor, Z. A. (2016), Evaluation of wave delivery methodology for brain MRE: Insights from computational simulations. Magn Reson Med. , which has been published in final form at http://dx.doi.org/10.1002/mrm.26333. This article may be used for non-commercial purposes in accordance with Wiley Terms and Conditions for Self-Archiving (http://olabout.wiley.com/WileyCDA/Section/id-828039.html)

Reuse
Items deposited in White Rose Research Online are protected by copyright, with all rights reserved unless indicated otherwise. They may be downloaded and/or printed for private study, or other acts as permitted by national copyright laws. The publisher or other rights holders may allow further reproduction and re-use of the full text version. This is indicated by the licence information on the White Rose Research Online record for the item.

Takedown
If you consider content in White Rose Research Online to be in breach of UK law, please notify us by emailing eprints@whiterose.ac.uk including the URL of the record and the reason for the withdrawal request.

UNIVERSITY OF LEEDS
University of Sheffield
UNIVERSITY of York

Evaluation of Wave Delivery Methodology for Brain MRE: Insights from Computational Simulations

Deirdre M. McGrath[1,2*]

Nishant Ravikumar[1]

Leandro Beltrachini[1]

Iain D. Wilkinson[2]

Alejandro F. Frangi[1]

Zeike A. Taylor[1]

[1]CISTIB Centre for Computational Imaging & Simulation Technologies in Biomedicine,

INSIGNEO Institute for *in silico* Medicine,

The University of Sheffield,

Sheffield,

UK

[2] Academic Unit of Radiology,

Faculty of Medicine, Dentistry & Health,

The University of Sheffield,

Sheffield,

UK

Address of author for correspondence:

Deirdre McGrath,

Centre for Computational Imaging & Simulation Technologies in Biomedicine (CISTIB),

Department of Electronic and Electrical Engineering,

The University of Sheffield,

C14, Pam Liversidge Building,

Mappin Street,

Sheffield,

S1 3JD

Tel: 0114-2225398
d.mcgrath@sheffield.ac.uk

Note: A.F. Frangi and Z.A. Taylor are joint senior authors

Word count: 5,885

Running head: Simulation of cranial vibration during brain MRE to evaluate wave delivery methodologies

ABSTRACT

Purpose: Magnetic resonance elastography (MRE) of the brain is being explored as a biomarker of neurodegenerative disease such as dementia. However, MRE measures for healthy brain have varied widely. Differing wave delivery methodologies may have influenced this, hence finite element-based simulations were carried out to explore this possibility.

Methods: The natural frequencies of a series of cranial models were calculated, and MRE-associated vibration was simulated for different wave delivery methods at varying frequency. Displacement fields and the corresponding brain constitutive properties estimated by standard inversion techniques were compared across delivery methods and frequencies.

Results: The delivery methods produced widely different MRE displacement fields and inversions. Furthermore, resonances at natural frequencies influenced the displacement patterns. Two of the wave delivery methods (head-cradle and acoustic pillow) gave rise to lower inversion errors, e.g., at 90 Hz the error in the storage modulus was 11% less than for the bite-bar method.

Conclusion: Wave delivery has an important impact on brain MRE reliability. Assuming small variations in brain biomechanics, as recently reported to accompany neurodegenerative disease (e.g., 7% for Alzheimer's disease), the effect of wave delivery is important. Hence, a consensus should be established on the optimum methodology, to ensure diagnostic and prognostic consistency.

KEYWORDS: Magnetic resonance elastography; brain; skull; finite element modeling simulation; natural frequencies; dementia

INTRODUCTION

Magnetic resonance elastography (MRE) (1) is a non-invasive method for measuring the biomechanical properties of biological tissue. This is achieved by delivery of mechanical waves to the site of interest, and measurement of the resulting displacement field using MRI. Biomechanical properties, such as stiffness and viscosity, are reconstructed from the displacement field using inversion algorithms. MRE of the brain is currently being explored for the diagnosis of neurological and neurodegenerative disease such as dementia (2-11). This evaluation is complicated by the fact that the MRE measures obtained so far for healthy brain have varied widely (12-15). In a review of healthy brain MRE data (12) the shear modulus values reported for white matter varied between 2.5 and 15.2 kPa, and for grey matter between 2.8 and 12.9 kPa. Additionally, some MRE studies have reported a dependency of brain elasticity and viscosity on age and gender (16,17). Moreover, the expected influence of neurodegenerative disease on brain biomechanics is low, e.g., in (2) only a 7% decrease in shear stiffness was reported for Alzheimer's disease compared with healthy controls.

While the variation in healthy brain MRE data may reflect true heterogeneity across populations, another possibility is that differences in methodology between studies had an influence, such as the wave delivery method and the excitation frequency employed. MRE waves are transmitted to the brain via vibration of the skull. However, as yet little is known about the motion of the cranium during this process, which is likely to depend on the mechanism of wave delivery, the wave frequency, and the specific characteristics and inter-subject variability of the anatomy of the skull. The mode of wave delivery has varied greatly between studies, e.g., bite bar (18), head cradle (16), and acoustic pillow (2). The wave frequency has also differed; however, as brain tissue exhibits viscoelastic properties, different viscoelastic moduli values are expected for different frequencies, and some studies have sought to characterize frequency-dependent effects (16,19,20).

Much previous work has been carried out using finite element model (FEM) based analysis to simulate motion of the human head during injury (21). Some studies have simulated or measured the natural frequencies (NFs) of the human skull, to predict the response of the skull to collision impact (22,23), to model the conduction of sound through the skull to aid hearing (24,25), or to understand skull vibration during surgical intervention (26). Recently, our group used steady state harmonic analysis to model MRE-associated wave propagation in the human brain to investigate the influence of reflections and heterogeneity across boundaries of anatomical structures, i.e., the processes of the *dura mater* and the ventricles (27). It was found that this anatomy influenced the displacement fields and led to error artifacts in the inversion calculation of the brain biomechanical properties. In this earlier work, to simplify the modeling of wave delivery to the brain, the skull was not included in the model, and vibration delivery was modeled from the *pia mater* of the brain using displacement loading with a uniform direction and magnitude. However, this simplification also excludes the possibility of modeling the effects of different skull excitation approaches.

In the current study it was sought to extend our FEM simulation framework to model the vibration dynamics of the skull during MRE, and thereby to determine their dependency on the wave delivery approach and frequency. Moreover, it was sought to determine the impact of varying wave delivery at the skull on the MRE displacement field in the brain, and on the derived biomechanical properties. The hypothesis was that the method of wave delivery and wave frequency would lead to different vibration fields in the skull and therefore in the brain, which would in turn influence the estimation of the biomechanical properties of the brain. As a preliminary step, modal analysis was carried out to understand the influence of the skull's various anatomical features on its natural frequencies and associated modes of vibration. To the best of our knowledge, this is the first report addressing the modeling of vibration dynamics of the whole human head during MRE.

METHODS

Overview of FEM simulations

All simulations were carried out using Abaqus v6.12 (Dassault Systèmes Simulia Corp, Johnston, RI, USA), and details are listed in Table 1.

Modal analysis to determine natural frequencies

FEM-based natural frequency (modal) analysis was carried out on skull-only models and a full head model derived from the XCAT phantom (28). The purpose of this investigation was to gain understanding of the influence of different anatomical components on cranial vibration. Varying material properties and different boundary conditions were also compared. Furthermore, for inter-subject comparison, modal analysis was carried out on a skull-only model derived from CT data.

Harmonic analysis to predict MRE wave propagation patterns

MRE wave propagation was simulated using harmonic analysis with the XCAT and CT derived models to investigate how skull vibration changes with wave delivery method and frequency. Comparison of the skull-only and full head XCAT models gives insight into the influence of the soft tissues on cranial vibration. Moreover, the full head model allows simulation of the complete propagation of vibrations from the skull to the brain, as desired, and exploration of the influence of wave delivery modes and frequency on brain displacement fields and, thereby, recovered tissue properties.

Models derived from the XCAT phantom (XM)

A set of skull models and a full head model were derived from the XCAT phantom (28) (XM1-XM6, Fig. 1). Surface meshes from the phantom were first interpolated onto a regular grid to create individual segmentations for the included anatomical structures. For the full head model, the segmentations were assigned different labels and merged to create a single multi-label segmentation. Next, a volumetric (tetrahedral) finite element mesh was generated in Matlab (R2012a, Mathworks Inc., Natick, MA) using the ISO2MESH software package (29). The volumetric mesh generation algorithm used within ISO2MESH is based on the CGAL library (CGAL, Computational Geometry Algorithms Library, cgal.org). The primary advantage of generating a volumetric mesh from a multi-label segmentation in this manner is the automatic generation of shared nodes between adjacent structures. Additionally, the ISO2MESH package provides user control over the tetrahedral element size to be applied to each region in the mesh, for computational efficiency.

The XM models included various combinations of anatomical components, to evaluate their respective influences (Fig. 1). XM1: upper skull, excluding jaw and neck; XM2: upper skull including jaw, but excluding neck; XM3: upper skull, plus jaw and neck. The upper skull contained a cavity corresponding to the sinuses. For models XM1-XM3 all bone was assigned properties as for cortical bone (see section: "Tissue material properties"). XM4: a further refined model was generated from XM3, in which extra structures were defined at the connection points of the jaw with the skull, and assigned material properties as for cartilage (two versions: Cartilage #1 and Cartilage #2 in Table 2). XM5: this model was a refinement of XM4 in which the upper skull and jaw included inner regions of cancellous bone. The cancellous bone was added using ISO2MESH by eroding the skull volume, while avoiding intersections with the sinuses. The erosion was performed until a realistic geometry for the cancellous bone was obtained, as assessed by visual comparison with the Colin 27 atlas segmentation (30).

XM6 was a refinement of XM5 in which additional regions were added: 1) brain in the inner skull cavity; 2) a layer of cerebrospinal fluid (CSF) surrounding the brain to approximate the meninges; 3) a volume to define the ventricles inside the brain, filled with CSF; 4) the processes of the *dura mater*, the *falx cerebri* and the *tentorium and falx cerebelli* membranes (denoted "FTM"), which lie between the hemispheres of the cortex, between the cortex and the cerebellum, and between the hemispheres of the cerebellum, respectively; 5) a single volume for the tissues (skin, muscle, fat, etc.) surrounding the skull and neck; and 6) the section of spinal cord on the inside of the neck. The *meninges* and FTM were not included in the original XCAT phantom data but were added based on estimations informed by manual segmentations of other anatomical MRI data. The approximate volume of the finite elements of the brain, CSF and FTM meshes matched that of the equivalent meshes employed in (27) (i.e., ≤ 2 mm^3), while, for computational efficiency, the other structures were modeled with a lower element density (i.e., element volume ≤ 4 mm^3). As the brain and CSF regions were modeled as near incompressible material, they were meshed with hybrid (linear-pressure) elements, which discretize and solve for the pressure field independently of the displacements, to avoid volumetric locking.

Skull model derived from CT data (CTM)

To explore the generality of the findings for the XCAT skull, a second skull model was prepared. This model (CTM, Fig 2a) was generated from a probabilistic atlas derived from the computed tomography (CT) images of patients (n=33), provided in a public domain database for computational anatomy (imagenglab.com/pddca_18.html). The probabilistic atlas was used as it represents the average skull shape for a population, and hence describes a more general anatomy. Additionally, in comparison to the raw patient CT images, the atlas is less noisy and hence easier to process. The skull was segmented semi-automatically from the atlas using ITK-SNAP (31). The segmentation process involved a combination of intensity thresholding and geodesic active contour propagation to segment the skull (including the jaw) and the first three vertebrae. A volumetric mesh was subsequently generated from the skull segmentation, similarly to the preparation of the XM models. The model included the skull, jaw and neck and a gap for the sinuses, and the material properties of elastic cortical bone were employed for the whole skull (i.e., no cartilage or cancellous bone included).

Tissue material properties

All tissue constitutive properties are summarized in Table 2. Cortical bone and cancellous bone were modeled initially as linear elastic solids with properties as defined in (32). Viscous damping was later added to both, in accordance with (33). Brain was modeled as a soft homogeneous isotropic linear viscoelastic near-incompressible material, with storage (G') and loss (G'') moduli values taken from MRE measurements in healthy brain at 25-90 Hz (16,18) and the density was approximated to that of water (1,000 kg/m^3) (16). The Poisson's ratio was set to 0.499999; estimated using the approximate speed of sound in the brain (1,550 ms^{-1}). Cerebrospinal fluid (CSF) in the meninges and ventricles was modeled as a soft viscoelastic solid (32). All other tissues were modeled as linear elastic solids, with parameters taken from the following sources: cartilage Young's modulus and density were estimated from (34), and two different Poisson's ratio values (0.5 and 0.1) were assumed to explore the effect of varying the cartilage properties, and thereby influencing the range of relative movement between the jaw and skull; tissues surrounding the skull and neck (skin, muscle, fat, etc.) were modeled as a uniform volume with properties of the scalp used in (32); spinal cord was modeled as a linear elastic solid, with the elastic modulus taken from (35), with an approximated Poisson's ratio and density; and the processes of the FTM were assigned properties from (24).

Boundary conditions

Different boundary conditions (BC) were applied for the various simulations (Table 1, Fig. 1). BC1: free boundaries; BC2: for models XM1 and XM2, in which the neck was excluded, nodes near to where the neck would attach to the skull were tethered (x, y and z displacements set to zero); BC3: for models including the neck (XM3-XM6), a set of nodes at the base of the neck were tethered; BC4: for XM6 the nodes at the end of the outer tissue of the neck were also tethered to approximate the connection of the neck to the rest of the body, and to reduce the reflection of wave energy back from the end surface of the neck tissue.

Modal analysis

The natural frequencies (or eigenfrequencies) of vibration were calculated in Abaqus by eigenvalue extraction using the Lanczos eigensolver. This analysis was carried out for each XM model and material combination with varying BCs (see Table 1), and for CTM with cortical bone only and BC3. The first six NFs were compared for the models XM1-XM6 and CTM.

MRE wave propagation simulation

MRE-associated mechanical vibration at specific frequencies was simulated in Abaqus using the direct-solution steady-state dynamic analysis (hereafter referred to as harmonic analysis). This is a perturbation procedure in which the response of a model to an applied harmonic vibration is calculated about a base state, to produce frequency-space steady-state nodal displacements **u**:

$$\mathbf{u}\,(\mathbf{x}\,,t) = \mathbf{u}(\mathbf{x})\exp\,(i\omega t) \tag{1}$$

where ω is the angular frequency, and **x** and t are spatial and temporal coordinates, respectively.

Using models XM5, XM6 and CTM, MRE simulation was carried out for frequencies at 5 Hz intervals in the range 5-150 Hz, and additionally at 37.5 and 62.5 Hz, to correspond with the frequencies included in the brain material specification (Table 2). Human brain MRE is usually carried out at <100 Hz, as brain exhibits viscoelastic behavior and strongly attenuates the MRE waves at higher frequencies, resulting in low displacement amplitudes and poor data quality. The upper limit of 150 Hz was chosen here to investigate effects in the vicinity of 100 Hz.

Displacement loading with an amplitude of 10 µm (chosen to approximate wave amplitudes observed in brain MRE) was delivered to sets of nodes at different positions on the skull surface corresponding to the different brain MRE wave delivery methods (Fig. 2): L1: "head-cradle" (16), temples vibrated in the head-foot direction; L2: temples vibrated left-right in opposite directions; L3: temples vibrated left-right in the same direction; L4: "acoustic pillow" (2), nodes at the back of the skull vibrated in anterior-posterior direction; L5: "bite bar" (18), nodes on upper and lower jaw vibrated in left-right direction. For consistency of wave delivery between XM5 and XM6, the loading was delivered to the skull surface in XM6 rather than the outer skin surface.

The vibration fields in the skull and brain were compared for the different loading options. The viscoelastic moduli (G' and G'') were reconstructed using direct inversion (27). This algorithm was implemented in Matlab through derivative calculation using a finite difference method on a "virtual imaging voxel" grid, which was interpolated at 3 mm intervals from the FE nodal displacements. To evaluate the inversion accuracy, the mean absolute percentage difference (MAPD) was calculated for the total brain volume:

$$MAPD = \frac{100}{N}\sum_{n}^{N}\left|\frac{G_{gt}-G_{i}^{n}}{G_{gt}}\right| \qquad (2)$$

where *N* is the total number of voxels, *n* is the voxel number, G_{gt} the ground truth value (of G' or G'') and G_i^n the inversion value. For selection of the volume corresponding to the full brain, a 3D mask was created. The voxels at the edge of the brain are affected by various sources of error, including averaging with the surrounding tissues from interpolation, derivative calculation, smoothing of the curl vector field during inversion, errors in the direct inversion caused by tissue heterogeneity and interference patterns resulting from wave reflections at tissue boundaries (27). Hence the MAPD was also calculated using a mask eroded by a margin of 3 voxels. By excluding this margin, understanding can be gained of the specific influence of the errors at the brain tissue edges.

RESULTS

Natural frequencies of the XCAT skull models

The first six (non-zero) NFs of the XCAT skull models are listed in Table 3. (For all models with BC1 the first six vibration modes will always, trivially, be rigid body modes, with theoretical frequencies of 0 Hz; only frequencies for non-rigid modes, i.e., non-zero frequencies, were included in Table 3).

For simulations #1-#6 (models XM1-XM3 with varying BCs) all of the first six non-zero NFs differ widely between simulations, indicating the influence of the various anatomical components and the boundary conditions. For simulation #6 (XM3, BC3) the first four NFs are 54, 82, 124 and 281 Hz. Visualization of the associated displacement fields revealed that the first three NFs are associated with the directions of rotation of the head about the neck, while the fourth NF was associated with motion of the jaw (Fig. 2g-j). For simulation #7 (XM4 with Cartilage #1, BC3) the first three NFs are unchanged, while NF#4 and subsequent NFs were altered. For simulation #8 (XM4, Cartilage #2, BC3) the first three NFs were again unchanged, while NF#4 and subsequent NFs were again altered. For XM5, with the addition of cancellous bone (simulation #9, BC3), all the NFs are slightly altered, while the first four are still associated with the same modes of vibration (Fig. 2g-j). With the addition of viscosity to the cortical and cancellous bone (simulation #10) the first six NFs are unaltered. For the XM6 full head model (simulation #11, BC3+BC4), the NF calculation was strongly influenced by the soft brain tissue, and resonances occurred at intervals of approximately 1 Hz, from the minimum NF 15.4 Hz.

Hence the inclusion or exclusion of the jaw and neck had a major impact on skull vibration, as did the boundary condition of tethering at the base of the neck. Based on the results of this analysis, for the MRE simulation in the skull and whole head models it was deemed necessary to include the jaw and neck and tethering at the base of the neck.

Effect of wave delivery and frequency on displacement fields in skull-only models

In Figure 3 the mean displacement components in the x, y and z directions (see Fig. 1 for the axes orientations) and the displacement vector magnitude are compared for the different MRE wave delivery methods (loading, L) and frequencies for XM5 and CTM. The plots demonstrate that resonances occur at the NFs of the models. However, for the various loading options, different resonance peaks are present or absent, depending on the direction of motion of the skull prescribed and controlled by the loading. For example, for XM5 with L1 (Fig. 3(a)), a peak occurs for the displacements in the x and y directions around 125 Hz, which corresponds to NF#3 at 127 Hz, while peaks for NF#1 and NF#2 are absent. For CTM with L1 (Fig. 3(b)), no resonance peaks are visible; however, there appears to be a gradual increase towards a peak, which would occur at the higher frequency of 230 Hz for NF#3. For XM5 with L2 (Fig.3(c)), a resonance peak occurs for the y and z components at 55 Hz, corresponding to NF#1 of 55 Hz, while for CTM (Fig. 3(d)), resonance is apparent around 115 Hz, corresponding to the NF#1 of CTM. There are similar patterns of particular resonances occurring for the other wave delivery options (L3-L5). Furthermore (outside of the resonance peaks) for each wave delivery method, displacement is predominantly in a single direction (x, y or z) corresponding to the direction of loading to the skull. It is also of importance to note that the different loading methods achieve different displacement amplitudes (x, y and z) and magnitudes (in Fig. 3 the y-axes are scaled differently for each plot for the benefit of clear depiction of the resonance peaks). For example at 37.5 Hz (outside resonance) the mean displacement magnitudes of XM5 for L1-L5 are: 20 µm; 7 µm; 9 µm; 9 µm; 7 µm. For CTM at 37.5 Hz similar mean displacements magnitudes were observed for L1-L5: 17 µm; 5 µm; 8 µm; 10 µm; 7 µm.

Figure 4 presents the displacement magnitudes plotted on the skull surface for XM5 for the various loading methods. In each case, vibration is shown at resonance, and for an example non-resonant frequency. The displacement fields differ between loading methods. Additionally, for each method, the displacement field alters greatly at resonance, when it resembles that of the corresponding eigenmode (Fig. 2g-i). The color scales of Fig. 4 are scaled differently for each plot, for the purpose of clear depiction of the displacement patterns, and ready comparison with the eigenmodes (Fig. 2g-i).

Effect of wave delivery and frequency on MRE displacement fields and inversions in XM6

Figure 5 presents plots of the mean displacements (x, y, z and magnitude) in the skull and brain of the XM6 model for the different loading methods and frequencies. For the skull, the displacement components again differ in magnitude, and the predominant direction varies with the wave delivery direction. Furthermore, resonance peaks whose frequencies lie within about 10 Hz of resonances for the XM5 (skull-only) model (Fig. 3) are visible. The relative proportions of the displacement components in the skull are mirrored in the displacement components of the brain, and likewise the brain resonance peaks occur in the vicinity of the resonances in the skull. Figure 5f compares the displacement magnitudes between the loading methods, revealing that for the same (10 µm) displacement loading on the skull surface, L1 achieved the highest displacement amplitudes in the skull and brain, while L2 achieved the lowest (e.g., at 50 Hz, the mean displacement magnitude in the brain was 26 µm for L1 and 5 µm for L2).

Figure 6 displays the displacement fields and inversion results for a central axial brain slice of XM6 at 50 and 90 Hz. The wave patterns for the different displacement components differ widely between loading methods and frequencies. The frequencies of 50 and 90 Hz were chosen as more generally representative of the loading methods, as they lie outside the resonance peaks for all methods. They also are two of the frequencies for which G' and G'' are specified for the brain material (Table 2). Loading methods L1 and L4 gave rise to similar patterns in the x, y and z displacement fields and in the inversion results, which is perhaps to be expected, as both methods result in a similar nodding motion of the head. Correspondingly, methods L3 and L5, which both prescribe a left-right motion of the head, also resulted in similar displacement field patterns and inversion results. Conversely, L2 resulted in very different displacement patterns from all the other methods, though the patterns of errors in the inversion results are similar to those of L3 and L5.

Figure 7 presents plots of mean G' and G'' over the brain volume for the different wave delivery methods and frequencies, and MAPD of G' and G'' for the full and eroded brain volumes, for the five frequencies of the ground truth data (Table 2). At higher frequencies, G' varies between the methods by ~500 Pa (Fig. 7a), and G'' by ~300 Pa (Fig. 7b). To interpret the shape of the plots in Figs. 7a and 7b it is necessary to know the ground truth moduli that Abaqus employed in the simulations: for frequency-dependent viscoelastic materials, Abaqus interpolates parameters linearly within the range of specified frequencies (Table 2), and caps parameters at the bounding values outside of this range (i.e. at frequencies <25 Hz, the 25 Hz moduli are used, and at >90 Hz, the 90 Hz moduli are used).

The MAPD also varied between loading methods, e.g., at 90 Hz, MAPD of G' for L1 and L4 was approximately 11% less than for L3 and L5, while for G'' at 37.5 Hz, it was approximately 17% lower for L1 and L4 compared with L3. For the eroded volume, the MAPDs are vastly reduced, though L1 and L4 still have predominantly the lower error values, except at the higher frequencies (62.5 and 90 Hz). However, the differences between delivery methods for the eroded mask are only on the order of 1%.

DISCUSSION

Natural frequencies of XCAT and CTM skull models

The NF analysis of the skull models XM1-XM5 revealed important information on the influence of the various anatomical components on skull vibration. As the delivery of MRE waves to the brain is mainly achieved via transmission through the skull, it is important to determine the relevant NFs of the skull (i.e., those that lie in the typical frequency range for brain MRE: 20-100 Hz), and to understand the factors that influence the eigenmodes. The inclusion of the jaw and neck, and tethering at the base of the neck strongly influenced the vibration of the skull and the NFs.

The NFs differed between CTM and the matching XM3 model (simulations #6 and #12, Table 3). The material specifications were identical for these simulations, however the volume (and therefore mass) of CTM was lower than that of XM3. NFs typically scale inversely with the square root of the mass, and hence the NFs for CTM are higher than those for XM3. However, structural variation between the models will also influence modal dynamics. While the NFs vary between models, the modes of vibration for the first four NFs are the same for both models (Fig. 2g-j).

Previous investigators have sought to measure or simulate the vibration and NFs of the human skull. However the methodology has varied widely between studies: some simulations or measurements excluded the jaw (23) or the neck (26), or both (22), and while some measurements were carried out in dry skull models (26), others were made in live human subjects (24), or both (36,37), and therefore the reported NFs have also varied widely between studies. In (23) two FE skull models were compared: one excluding the jaw and neck, and the other excluding the jaw but including the neck. Tethering was also included at the base of the skull or neck. In (23) the range of the first four NFs for the model without the neck was 149.1-860.2 Hz, while the range of the first four NFs of the nearest corresponding model in this study (XM1 with BC2) was 321-1488 Hz. As in the present study, in (23) it was found that when the neck was included the NFs were reduced (first four: 88.9-399.4 Hz), and furthermore the rotational motion of the skull for the first three modes was similar to those observed in this study (Fig. 2g-j), while the fourth was associated with head-foot motion of the skull. However, in (23) they did not include the jaw bone, whereas in the present study it was found that the fourth NF was associated with jaw motion. Moreover, in this study for BC3, NF#4 was > 200 Hz for XM3 and > 400 Hz for CTM; as brain MRE is typically carried out at < 100 Hz, this suggests that jaw motion may have a smaller influence on the motion of the skull during MRE.

In this study the NFs of the full head model (XM6) were very different to those of the skull-only model (XM5). The XM6 modal analysis was strongly influenced by the soft brain tissue, and the different anatomical structures within the cranium, and NFs occurred at intervals of approximately 1 Hz, from the minimum NF of 15.4 Hz. This differed greatly from reported NFs for *in vivo* human head: Hakansson et al. (24) measured NFs in the range 500-7,500 Hz for *in vivo* human skulls and found 14-19 resonances, with the average of the two lowest frequencies at 972 Hz. Cai et al. (36) also made *in vivo* measurements in the range 2-52 kHz and made a comparison with dry skulls. They found complex resonances and antiresonances in both the dry skulls and live head, which were strongly dependent on the transducer position, and found that damping in the live head reduced the resonance peaks.

The effect of damping from soft tissues could be observed in the MRE simulation with XM6, as the resonance peaks were shifted with respect to the XM5 skull-only model (Figs. 3 and 5). Furthermore, the MRE simulation could explore the effect of delivering wave energy at different positions, and the associated vibration effects of each delivery mode. Hence, for XM6 the MRE simulations were more informative than the modal analysis.

Inter-subject differences in skull NFs and possible implications for MRE

The different NFs of the XM3 and CTM models indicate that the NFs will change between individuals depending on the size and shape of the skull. The different resonance effects in the MRE simulations of XM5 and XM6 also indicate how NFs will shift due to the damping effects of the tissues in the head, and this is likely to vary between individuals. According to the *in vivo* measurements of (24,36), the NFs of the *in vivo* human head are likely to occur at > 500 Hz, which is well outside the typical frequencies employed for brain MRE, i.e., 20-100 Hz. However, the simulations in this study have demonstrated that when resonances do occur at or in the vicinity of the MRE excitation frequency they can have a major impact on the wave fields in the brain. Hence, it is the recommendation of this study that further exploration should be carried out with volunteers to determine the resonances of the human head and the impact of these on the MRE measurements.

Implications of the choice of wave delivery method and frequency in brain MRE

The results of this study have proven the hypothesis that, in the context of simulation, MRE wave delivery methodology and frequency affect the displacement fields in the skull and brain, and also the inversion accuracy. Different displacement components were dominant for the different methods, while some methods had similar patterns of displacement and inversion error, i.e., L1 was similar to L4, and L3 was similar to L5. Furthermore, if the NFs lie at or close to the MRE wave frequency, a resonance peak can occur in the MRE displacement fields. Also, only particular NF resonances occur for the different loading methods, and the peaks can accentuate the differences between displacement components. For accurate inversion it is important to have balance between the displacement components in order to achieve full rank in the system of equations solved in the direct inversion (38). Hence, large disparities between displacement components caused by a particular wave delivery or resonances may lead to inaccurate inversion.

Overall L1 (head-cradle) and L4 (acoustic pillow) produced the lowest errors in the inversions. In Fig. 6, the inversion errors appear to be mainly associated with interaction of the wave field with the *falx cerebri* membrane, as large inversion errors occur at either side of this structure (see last panel in Figure 1 for location of the *falx cerebri* in an axial slice through the brain). For methods L1 and L4 the displacement field is moving predominantly in a direction parallel to the *falx* (y-direction), while for the other methods the dominant motion is left-right (x-direction), and lesser artifacts occur for L1 and L4 (especially at 50 Hz, Fig. 6). In our previous brain MRE simulation work (27) it was found that inversion artifacts occurred close to interfaces between brain tissue and the FTM and ventricles. The conclusion of that earlier study was that errors at the boundaries were caused by a combination of factors: 1) reflection, refraction and scattering at tissue boundaries leading to wave interference, which results in inversion artifacts at larger sampling steps (3 mm); 2) material heterogeneity bringing about errors in the direct inversion algorithm (which assumes local homogeneity (38)); 3) averaging across the tissue boundaries due to interpolation, derivative calculations and smoothing of the curl vector field during the inversion (27). However, the findings of this present study emphasize the importance of wave reflection and the resulting interference patterns, as the different wave delivery methods produce different predominant directions of motion accompanied by different magnitudes of inversion error.

Limitations of the current study and future work

The major limitation of this study was the simplicity of the models employed, in terms of anatomy and material specifications. The approximations involved in the FE modeling and simulations were further limitations. For instance, the anatomical models employed were based on the anatomy of a single individual (XM) and on the average model of a small cohort (CTM), and therefore do not capture all the variability of anatomy across the population. Skull shape is likely to vary with factors such gender, age and race. Future work will investigate the variability of resonant frequencies across the population by means of statistical shape modeling of the skull based on a wider population of data. The models were also simplified in terms of the structures included and the material models used, such as a soft viscoelastic solid for CSF as opposed to a fluid. Furthermore, the *meninges* have in reality a complex structure: the *dura mater* (attached to the skull) is connected to the *pia mater* (attached to the brain) via filaments called *trabeculae* running through the *subarachnoid* space, which is permeated with CSF. A previous study measuring MRE wave transmission from the skull to brain (39) concluded that the *meninges* strongly attenuate MRE waves. Furthermore, other anatomical features in the head that were not included are likely to cause wave attenuation through viscosity and scattering at tissue interfaces, and indeed brain tissue itself is in reality heterogeneous (19), meaning waves are likely to be scattered at the interfaces of different brain regions (40). Furthermore, brain tissue is anisotropic (41), and this would influence MRE displacement fields. Future studies will explore the sensitivity of the findings of this work to variations in material properties of the different anatomical structures.

However, the variability that might occur between individuals and the approximations employed in the material modeling do not negate the overall findings of this work, i.e., that the choice of wave delivery methodology can influence brain MRE data. Rather, studies with wider populations and varied properties would provide a better estimate of the actual impact of using different wave delivery methods.

Although further simulations are warranted to explore the limitations of the findings of this study, ultimately *in vivo* MRE studies are required to determine the actual impact on varying wave delivery. Hence, the main recommendation from this work is that volunteer studies comparing MRE acquisitions with different wave delivery methods be undertaken. In fact, a recent study by Fehlner at al. (42) compared the head-cradle method (L1) with a newer remote excitation method and found that the magnitude and phase of the complex shear modulus could differ by as much as 6 and 13% respectively in the brain regions examined. Further similar studies should be carried out to determine a consensus methodology for optimum accuracy and stability, although patient comfort and the practicality of the method are other primary considerations.

CONCLUSIONS

Through simulation, this study has demonstrated that in brain MRE the method of wave delivery and wave frequency strongly influence the displacement fields in the skull and brain, and consequently the accuracy of the inversion reconstructions of the brain biomechanical properties (e.g., at 90 Hz an 11% lower inversion error for the head-cradle (L1) and acoustic-pillow (L4) compared with the bite bar (L5)). Furthermore, the natural frequencies of vibration of the head can influence the MRE displacement fields in the brain and therefore the inversion accuracy.

As the models employed in this study were generated from a limited representation of human head anatomy and were simplified in various aspects, future simulation studies are required to explore the limitations of these findings. Furthermore, it is recommended that *in vivo* MRE studies are made on volunteers using the various wave delivery methods and varying frequencies, to determine the stability of the measures of brain tissue biomechanics, and the possible influence of resonant frequencies.

ACKNOWLEDGEMENTS

This study was funded by the European Union’s Seventh Framework Programme (FP7/2007 – 2013) as part of the project VPH-DARE@IT (grant agreement no. 601055). There are no conflicts of interest associated with this work.

REFERENCES

1. Muthupuillai R, Lomas DJ, Rossman PJ, Greenleaf JF, Manduca A, Ehman RL. Magnetic resonance elastography by direct visualization of propagating acoustic strain waves. Science 1995;269(5232):1854-1857.
2. Murphy MC, Huston JI, Jack CRJ, Glaser KJ, Manduca A, Felmlee JP, Ehman RL. Decreased brain stiffness in Alzheimer's disease determined by magnetic resonance elastography. J Magn Reson Im 2011;34:494-498.
3. Wuerfel J, Paul F, Beierbach B, Hamhaber U, Klatt D, Papazoglou S, Zipp F, Martus P, Braun J, Sack I. MR-elastography reveals degradation of tissue integrity in multiple sclerosis. Neuroimage 2010;49:2520-2525.
4. Schregel K, Wuerfel E, Garteiser P, Gemeinhardt I, Prozorovski T, Aktas O, Merz H, Petersen D, Wuerfel J, Sinkus R. Demyelination reduces brain parenchymal stiffness quantified in vivo by magnetic resonance elastography. P NATL ACAD SCI USA 2012;109(17):6650-6655.
5. Murphy MC, Curran GL, Glaser KJ, Rossman PJ, Huston JI, Poduslo JF, Jack CRJ, Felmlee JP, Ehman RL. Magnetic resonance elastography of the brain in a mouse model of Alzheimer's disease: initial results. Magn Reson Imaging 2012;30:535-539.
6. Streitberger KJ, Sack I, Krefting D, Pfuller C, Braun J, Paul F, Wuerfel J. Brain viscoelasticity alteration in chronic-progressive multiple sclerosis. PLoS One 2012;7(1):e29888.
7. Freimann FB, Streitberger KJ, Klatt D, Lin K, McLaughlin J, Braun J, Sprung C, Sack I. Alteration of brain viscoelasticity after shunt treatment in normal pressure hydrocephalus. Neuroradiology 2012;54(3):189-196.
8. Streitberger KJ, Wiener E, Hoffmann J, Freimann FB, Klatt D, Braun J, Lin K, McLaughlin J, Sprung C, Klingebiel R, Sack I. In vivo viscoelastic properties of the brain in normal pressure hydrocephalus. NMR Biomed 2011;24(4):385-392.
9. Lipp A, Trbojevic R, Paul F, Fehlner A, Hirsch S, Scheel M, Noack C, Braun J, Sack I. Cerebral magnetic resonance elastography in supranuclear palsy and idiopathic Parkinson's disease. Neuroimage Clin 2013;3:381-387.
10. Riek K, Millward JM, Hamann I, Mueller S, Pfueller CF, Paul F, Braun J, Infante-Duarte C, Sack I. Magnetic resonance elastography reveals altered brain viscoelasticity in experimental autoimmune encephalomyelitis. Neuroimage Clin 2012;1(1):81-90.
11. Huston J, 3rd, Murphy MC, Boeve BF, Fattahi N, Arani A, Glaser KJ, Manduca A, Jones DT, Ehman RL. Magnetic resonance elastography of frontotemporal dementia. J Magn Reson Imaging 2015.

12. Di Ieva A, Grizzi F, Rognone E, Tse ZT, Parittotokkaporn T, Rodriguez YBF, Tschabitscher M, Matula C, Trattnig S, Rodriguez YBR. Magnetic resonance elastography: a general overview of its current and future applications in brain imaging. Neurosurg Rev 2010;33(2):137-145; .
13. Glaser KJ, Manduca A, Ehman RL. Review of MR elastography applications and recent developments. J Magn Reson Im 2012;36(4):757-774.
14. Kruse SA, Rose GH, Glaser KJ, Manduca A, Felmlee JP, Jack CR, Jr., Ehman RL. Magnetic resonance elastography of the brain. Neuroimage 2008;39(1):231-237.
15. Chatelin S, Constantinesco A, Willinger R. Fifty years of brain tissue mechanical testing: from in vitro to in vivo investigations. Biorheology 2010;47(5-6):255-276.
16. Sack I, Beierbach B, Wuerfel J, Klatt D, Hamhaber U, Papazoglou S, Martus P, Braun J. The impact of aging and gender on brain viscoelasticity. Neuroimage 2009;46(3):652-657.
17. Arani A, Murphy MC, Glaser KJ, Manduca A, Lake DS, Kruse SA, Jack CRJ, Ehman RL, Huston JI. Measuring the effects of aging and sex on regional brain stiffness with MR elastography in healthy older adults. Neuroimage 2015;111:59-64.
18. Green MA, Bilston LE, Sinkus R. In vivo brain viscoelastic properties measured by magnetic resonance elastography. NMR Biomed 2008;21(7):755-764.
19. Guo J, Hirsch S, Fehlner A, Papazoglou S, Scheel M, Braun J, Sack I. Towards an elastographic atlas of brain anatomy. PLoS One 2013;8(8):e71807.
20. Dittmann F, Hirsch S, Tzschätzsch H, Guo J, Braun J, Sack I. In vivo wideband multifrequency MR elastography of the human brain and liver. Magn Reson Med 2015:Epub 10.1002/mrm.26006.
21. Tse KM, Lim SP, Tan VBC, Lee HP. A review of head injury and finite element head models. American Journal of Engineering, Technology and Society 2014;1(5):28-52.
22. Nickell RE, Marcal PV. In-vacuo modal dynamic response of the human head. J Eng Ind - T ASME 1974;96(2):490-494
23. Huang BW, Ou Y-W, Chang CH, Chen GS, Yen KY, Tseng J-G. Dynamic characteristics of the skull with the neck effect. Life Sci J 2013;10(2):265-270.
24. Hakansson B, Brandt A, Carlsson P, Tjellstrom A. Resonance frequencies of the human skull in vivo. J Acoust Soc Am 1994;95(3):1474-1481.
25. Kim N, Chang Y, Stenfelt S. A three-dimensional finite-element model of a human dry skull for bone-conduction hearing. Biomed Res Int 2014;2014:519429.
26. Huang BW, Kung HK, Chang K-Y, Hsu PK, Tseng J-G. Human Cranium Dynamic Analysis. Life Sci J 2009;6(4):15-22.

27. McGrath DM, Ravikumar N, Wilkinson ID, Frangi AF, Taylor Z. Magnetic resonance elastography of the brain: An in silico study to determine the influence of cranial anatomy. Magn Reson Med 2015;doi: 10.1002/mrm.25881.

28. Segars WP, Sturgeon G, Mendonca S, Grimes J, Tsui BM. 4D XCAT phantom for multimodality imaging research. Med Phys 2010;37(9):4902-4915.

29. Fang Q, Boas D. Tetrahedral mesh generation from volumetric binary and gray-scale images. Proc IEEE Int Symp Biomed Imaging 2009:1142-1145.

30. Aubert-Broche B, Evans AC, Collins L. A new improved version of the realistic digital brain phantom. Neuroimage 2006;32(1):138-145.

31. Yushkevich PA, Piven J, Hazlett HC, Smith RG, Ho S, Gee JC, Gerig G. User-guided 3D active contour segmentation of anatomical structures: significantly improved efficiency and reliability. Neuroimage 2006;31(3):1116-1128.

32. Yang J. Investigation of brain trauma biomechanics in vehicle traffic accidents using human body computational models. A Wittek et al (eds), Computational biomechanics for medicine: Soft tissues and the musculoskeletal system, Springer 2011:5-14.

33. Ed. J Middleton GP, M L Jones. Computer methods in biomechanics and biomedical engineering - 2: CRC Press; 1999. 126 p.

34. Pal S. Design of artifical human joints and organs: Springer; 2014.

35. Bilston LE, Thibault LE. The mechanical properties of the human cervical spinal cord in vitro. Ann Biomed Eng 1996;24:67-74.

36. Cai Z, Richards DG, Lenhardt ML, Madsen AG. Response of human skull to bone-conducted sound in the audiometric-ultrasonic range. Int Tinnitus J 2002;8(1):3-8.

37. Franke EK. The response of the human skull to mechanical vibrations. Ohio, USA: Wright-Patterson Air Force Base 1954.

38. Honarvar M, Sahebjavaher R, Sinkus R, Rohling R, Salcudean S. Curl-based Finite Element Reconstruction of the Shear Modulus Without Assuming Local Homogeneity: Time Harmonic Case. IEEE Trans Med Imaging 2013.

39. Clayton EH, Genin GM, Bayly PV. Transmission, attenuation and reflection of shear waves in the human brain. J R Soc Interface 2012;9(76):2899-2910.

40. Papazoglou S, Xu C, Hamhaber U, Siebert E, Bohner G, Klingebiel R, Braun J, Sack I. Scatter-based magnetic resonance elastography. Phys Med Biol 2009;54(7):2229-2241.

41. Romano A, Scheel M, Hirsch S, Braun J, Sack I. In vivo waveguide elastography of white matter tracts in the human brain. Magn Reson Med 2012;68(5):1410-1422.

42. Fehlner A, Papazoglou S, McGarry MD, Paulsen KD, Guo J, Streitberger KJ, Hirsch S, Braun J, Sack I. Cerebral multifrequency MR elastography by remote excitation of intracranial shear waves. NMR Biomed 2015;28:1426-1432.

Table 1 Simulation details

Simulation No.	NF/MRE	Model	No. of Elements	Element volume	Boundary conditions and loading	Materials
1	NF	XM1	823001	≤ 2 mm^3	BC1	Cortical bone
2	NF	XM1	823001	≤ 2 mm^3	BC2	Cortical bone
3	NF	XM2	779408	≤ 2 mm^3	BC1	Cortical bone
4	NF	XM2	779408	≤ 2 mm^3	BC2	Cortical bone
5	NF	XM3	838627	≤ 2 mm^3	BC1	Cortical bone
6	NF	XM3	838627	≤ 2 mm^3	BC3	Cortical bone
7	NF	XM4	838627	≤ 2 mm^3	BC3	Cortical bone + cartilage #1
8	NF	XM4	838627	≤ 2 mm^3	BC3	Cortical bone + cartilage #2
9	NF	XM5	838627	≤ 2 mm^3	BC3	Cortical + cancellous bone + cartilage #2
10	NF	XM5	838627	≤ 2 mm^3	BC3	Viscoelastic cortical viscoelastic cancellous bone + cartilage #2
11	NF	XM6	1420763	≤ 4mm^3 (brain, CSF and FTM ≤ 2 mm^3)	BC3+BC4	Viscoelastic cortical and cancellous bone, cartilage #2, outer head, brain, spinal cord, FTM, CSF
12	NF	CTM	712434	≤ 2 mm^3	BC3	Cortical bone
13	MRE (5-150 Hz)	XM5	838627	≤ 2 mm^3	BC3+L1	Viscoelastic cortical bone + viscoelastic cancellous bone+ cartilage #2
14	MRE (5-150 Hz)	XM5	838627	≤ 2 mm^3	BC3+L2	Viscoelastic cortical bone + viscoelastic cancellous bone+ cartilage #2
15	MRE (5-150 Hz)	XM5	838627	≤ 2 mm^3	BC3+L3	Viscoelastic cortical bone + viscoelastic cancellous bone+ cartilage #2
16	MRE (5-150 Hz)	XM5	838627	≤ 2 mm^3	BC3+L4	Viscoelastic cortical bone + viscoelastic cancellous bone+ cartilage #2

17	MRE (5-150 Hz)	XM5	838627	≤ 2 mm^3	BC3+L5	Viscoelastic cortical bone + viscoelastic cancellous bone+ cartilage #2
18	MRE (5-150 Hz)	CTM	712434	≤ 2 mm^3	BC3+L1	Cortical bone
19	MRE (5-150 Hz)	CTM	712434	≤ 2 mm^3	BC3+L2	Cortical bone
20	MRE (5-150 Hz)	CTM	712434	≤ 2 mm^3	BC3+L3	Cortical bone
21	MRE (5-150 Hz)	CTM	712434	≤ 2 mm^3	BC3+L4	Cortical bone
22	MRE (5-150 Hz)	CTM	712434	≤ 2 mm^3	BC3+L5	Cortical bone
23	MRE (5-150 Hz)	XM6	1420763	≤ 4 mm^3 (brain, CSF and FTM ≤ 2 mm^3)	BC3+BC4+L1	Viscoelastic cortical and cancellous bone, cartilage #2, outer head, brain, spinal cord, FTM, CSF
24	MRE (5-150 Hz)	XM6	1420763	≤ 4 mm^3 (brain, CSF and FTM ≤ 2 mm^3)	BC3+BC4+L2	Viscoelastic cortical and cancellous bone, cartilage #2, outer head, brain, spinal cord, FTM, CSF
25	MRE (5-150 Hz)	XM6	1420763	≤ 4 mm^3 (brain, CSF and FTM ≤ 2 mm^3)	BC3+BC4+L3	Viscoelastic cortical and cancellous bone, cartilage #2, outer head, brain, spinal cord, FTM, CSF
26	MRE (5-150 Hz)	XM6	1420763	≤ 4 mm^3 (brain, CSF and FTM ≤ 2 mm^3)	BC3+BC4+L4	Viscoelastic cortical and cancellous bone, cartilage #2, outer head, brain, spinal cord, FTM, CSF
27	MRE (5-150 Hz)	XM6	1420763	≤ 4 mm^3 (brain, CSF and FTM ≤ 2 mm^3)	BC3+BC4+L5	Viscoelastic cortical and cancellous bone, cartilage #2, outer head, brain, spinal cord, FTM, CSF

Table 2: Constitutive parameter values employed in simulations

<table>
<tr><td rowspan="2">Tissue type</td><td colspan="11">Parameter values</td></tr>
<tr><td colspan="3">Young's modulus (MPa)</td><td colspan="4">Poisson's ratio</td><td colspan="4">Density (kg/m^3)</td></tr>
<tr><td>Cortical bone</td><td colspan="3">15,000</td><td colspan="4">0.21</td><td colspan="4">1,900</td></tr>
<tr><td>Cancellous bone</td><td colspan="3">4,600</td><td colspan="4">0.05</td><td colspan="4">1,500</td></tr>
<tr><td>Cartilage #1</td><td colspan="3">1</td><td colspan="4">0.5</td><td colspan="4">1,100</td></tr>
<tr><td>Cartilage #2</td><td colspan="3">1</td><td colspan="4">0.1</td><td colspan="4">1,100</td></tr>
<tr><td>Outer head tissues</td><td colspan="3">16.7</td><td colspan="4">0.42</td><td colspan="4">1,000</td></tr>
<tr><td>Spinal cord</td><td colspan="3">1.02</td><td colspan="4">0.5</td><td colspan="4">1,000</td></tr>
<tr><td>FTM</td><td colspan="3">31.5</td><td colspan="4">0.45</td><td colspan="4">1,130</td></tr>
<tr><td rowspan="6">Brain</td><td colspan="3">Frequency (Hz)</td><td colspan="2">G' (Pa)</td><td colspan="2">G'' (Pa)</td><td colspan="4" rowspan="6">1,000</td></tr>
<tr><td colspan="3">25</td><td colspan="2">1110</td><td colspan="2">480</td></tr>
<tr><td colspan="3">37.5</td><td colspan="2">1310</td><td colspan="2">570</td></tr>
<tr><td colspan="3">50</td><td colspan="2">1520</td><td colspan="2">600</td></tr>
<tr><td colspan="3">62.5</td><td colspan="2">2010</td><td colspan="2">800</td></tr>
<tr><td colspan="3">90</td><td colspan="2">3100</td><td colspan="2">2500</td></tr>
<tr><td>CSF</td><td>G_0 (Pa)</td><td colspan="2">G_∞ (Pa)</td><td colspan="2">β (s^{-1})</td><td colspan="2">K (MPa)</td><td colspan="4" rowspan="2">1,000</td></tr>
<tr><td></td><td>1,000</td><td colspan="2">900</td><td colspan="2">80</td><td colspan="2">1,050</td></tr>
<tr><td rowspan="2">Viscous damping cortical bone</td><td>t (s)</td><td colspan="2">10</td><td colspan="2">10^2</td><td colspan="2">10^3</td><td colspan="2">10^4</td><td colspan="2">10^5</td></tr>
<tr><td>$G(t)/G_0$</td><td colspan="2">0.973</td><td colspan="2">0.95</td><td colspan="2">0.915</td><td colspan="2">0.853</td><td colspan="2">0.773</td></tr>
<tr><td rowspan="2">Viscous damping cancellous bone</td><td>t (s)</td><td>1</td><td>2</td><td>3</td><td>4</td><td>5</td><td>6</td><td>7</td><td>8</td><td>9</td><td>10</td></tr>
<tr><td>$G(t)/G_0$</td><td>0.93</td><td>0.9</td><td>0.888</td><td>0.873</td><td>0.865</td><td>0.875</td><td>0.852</td><td>0.834</td><td>0.74</td><td>0.7</td></tr>
</table>

Table 3: First six non-zero natural frequencies for simulations

Simulation details				Natural Frequencies					
No.	**Model**	**BC**	**Material Types**	**#1**	**#2**	**#3**	**#4**	**#5**	**#6**
1	XM1	BC1	Cortical bone	2747	3223	3733	3833	3998	4507
2	XM1	BC2	Cortical bone	321	459	817	1488	2348	2628
3	XM2	BC1	Cortical bone	341	846	1352	1837	2482	2726
4	XM2	BC2	Cortical bone	288	348	449	707	875	1356
5	XM3	BC1	Cortical bone	336	792	827	1350	1682	1839
6	XM3	BC3	Cortical bone	54	82	124	281	407	600
7	XM4	BC3	Cortical bone + cartilage #1	54	82	124	275	402	598
8	XM4	BC3	Cortical bone + cartilage #2	54	82	124	233	384	586
9	XM5	BC3	Cortical + cancellous bone + cartilage #2	55	84	127	233	387	578
10	XM5	BC3	Viscoelastic cortical and cancellous bone + cartilage #2	55	84	127	233	387	578
11	XM6	BC3+BC4	Viscoelastic cortical and cancellous bone, cartilage #2, outer head, brain, spinal cord, FTM, CSF	15.4	16.0	16.1	16.4	17.1	17.8
12	CTM	BC3	Cortical bone	115	127	230	406	974	1087

FIGURES

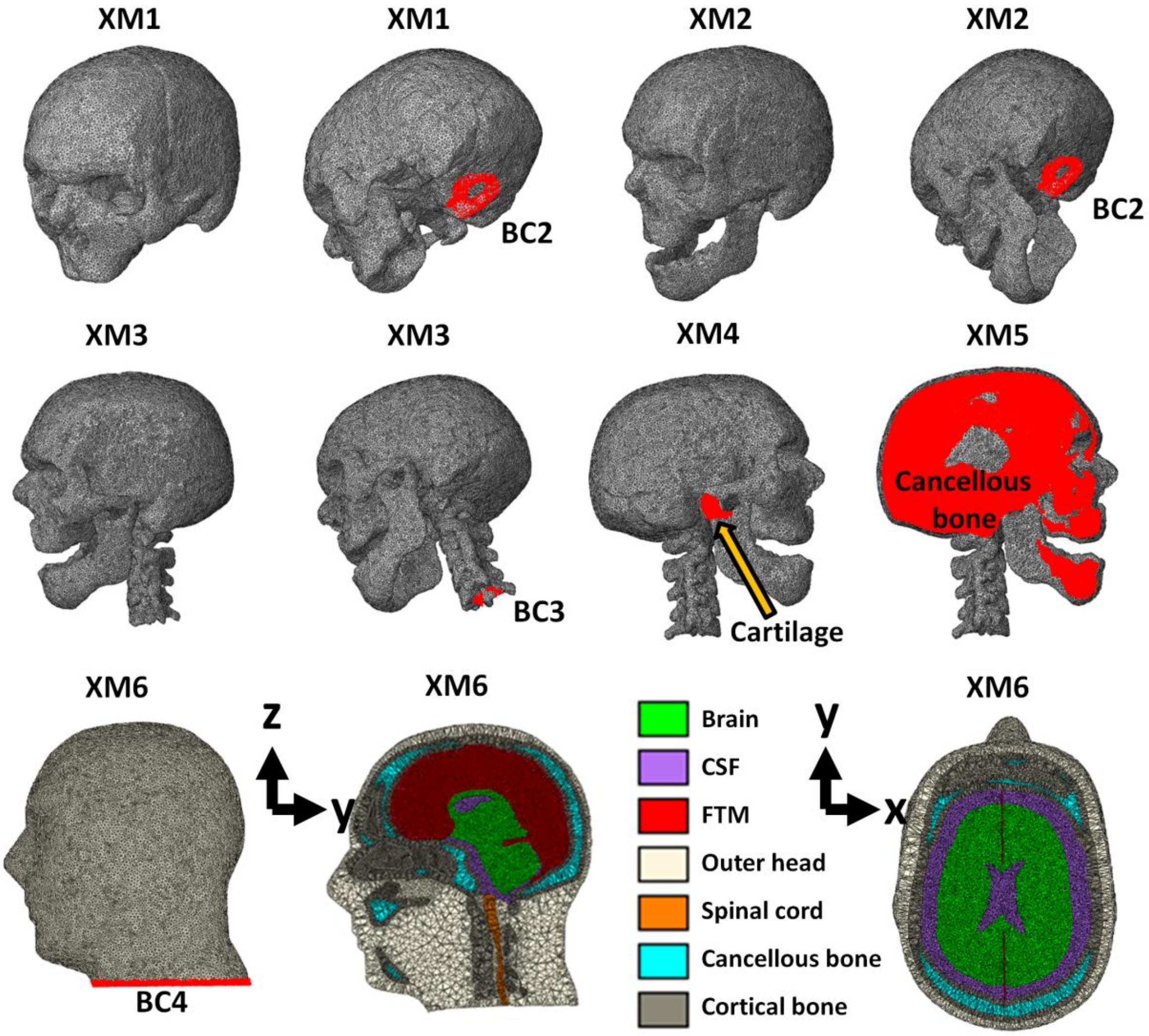

Figure 1: Models from XCAT phantom (XM) and boundary conditions (BC)

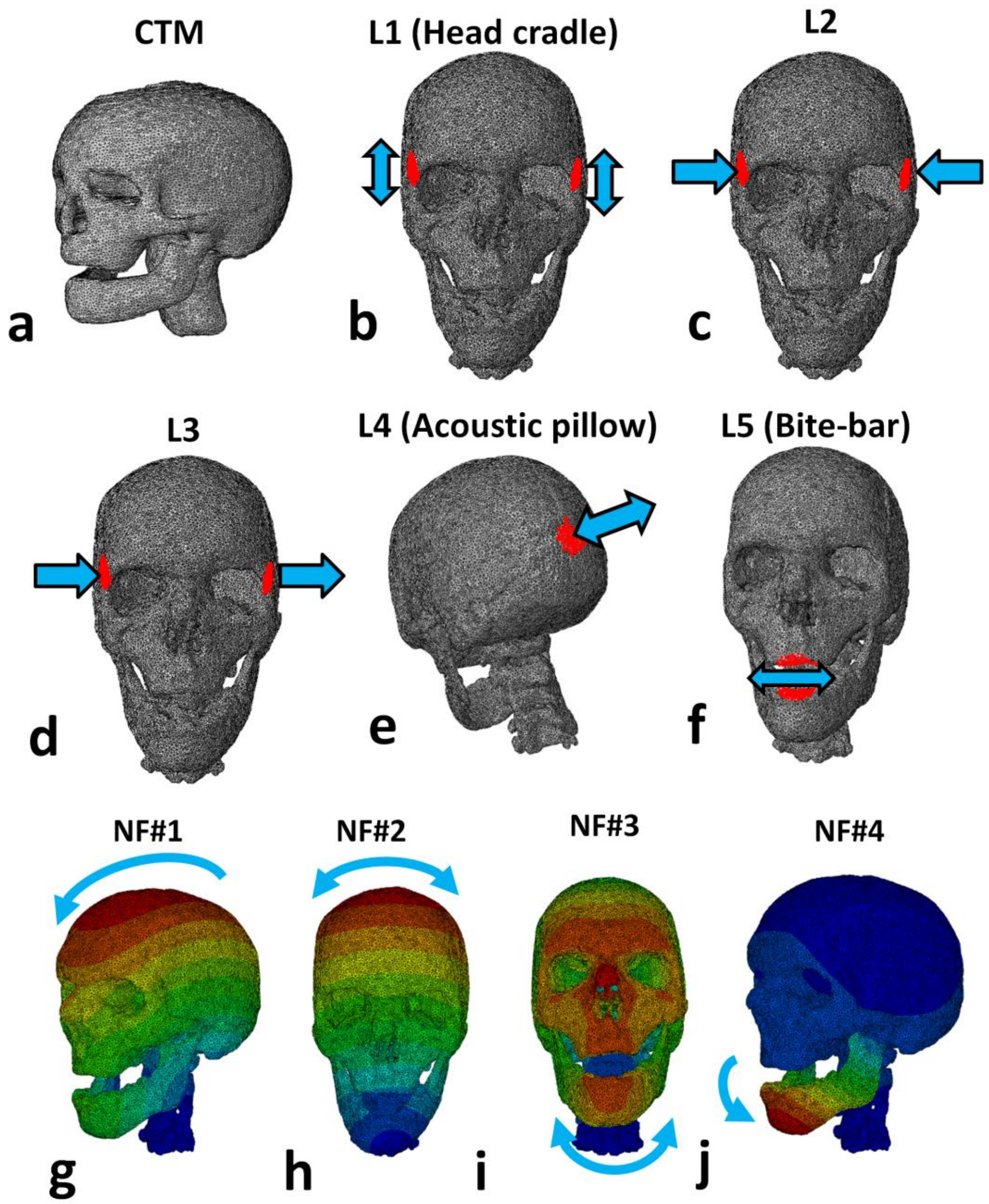

Figure 2: CTM model and loading (L) positions and directions displayed with XM3 model, and motion of skull associated with the first four natural frequencies (NF) of XM4 with BC3: a) CTM model; b) L1 or "head cradle", with temples vibrating in head-foot direction; c) L2 temples vibrating left-right in opposite directions; d) L3 temples vibrating left-right in same direction; e) L4 or "acoustic pillow", posterior of skull vibrating in anterior-posterior direction; f) L5 or "bite-bar", upper and lower jaw vibrating in left-right direction; g) NF#1; h) NF#2; i) NF#3; j) NF#4.

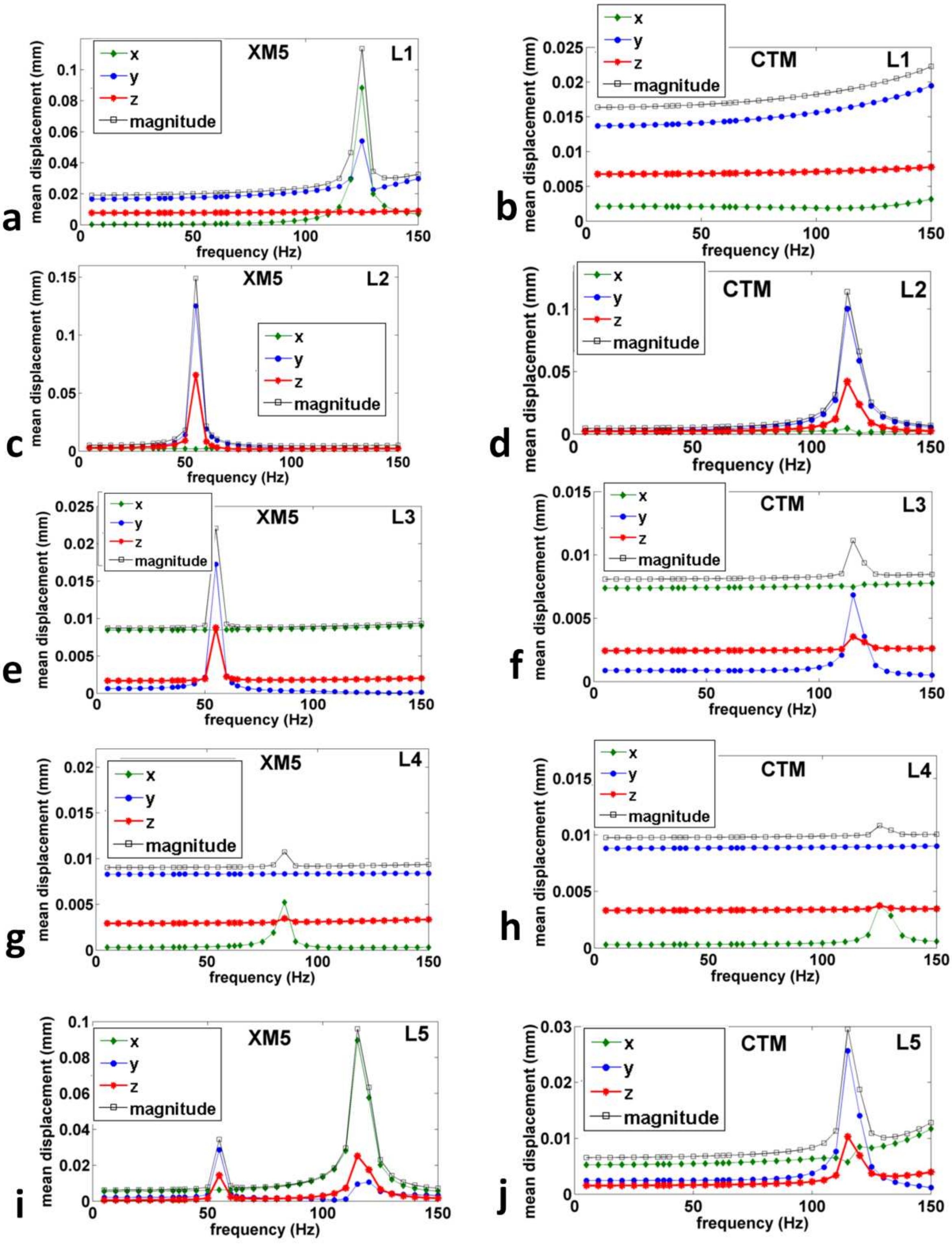

Figure 3: Comparison of mean x, y and z displacement components and overall displacement magnitudes against frequency for skull-only models XM5 and CTM for different wave delivery methods (loading, L): a) XM5 L1; b) CTM L1; c) XM5 L2; d) CTM L2; e) XM5 L3; f) CTM L3; g) XM5 L4; h) CTM L4; i) XM5 L5; j) CTM L5.

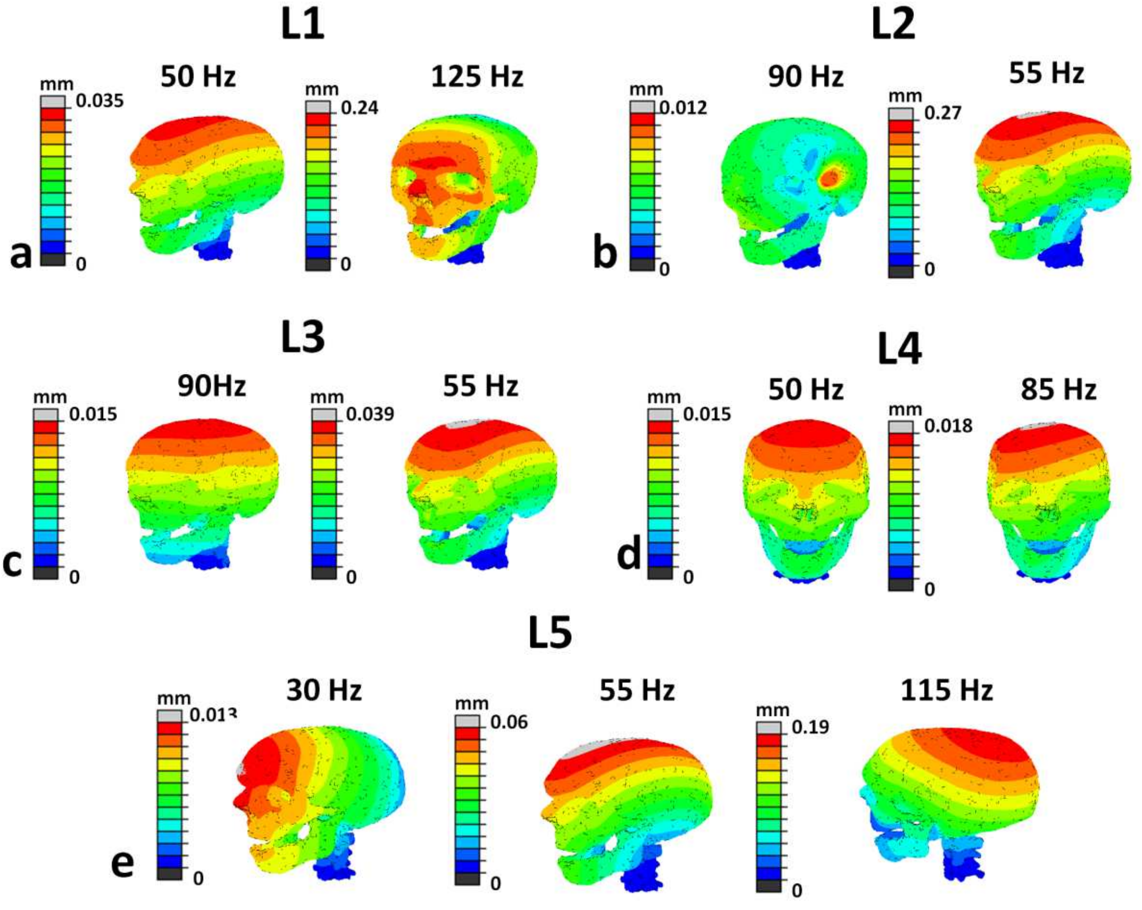

Figure 4: MRE simulation displacement magnitudes in XM5 model outside resonance and at the resonance peaks for different wave delivery methods (loading, L): a) L1, outside resonance at 50 Hz, and the resonance at 125 Hz; b) L2, outside resonance at 90 Hz, and the resonance at 55 Hz; c) L3, outside resonance at 90 Hz, and the resonance at 55 Hz; d) L4, outside resonance at 50 Hz, and at the resonance at 85 Hz; e) L5, outside resonance at 30 Hz, and at the first resonance at 55 Hz, and at the second resonance at 115 Hz.

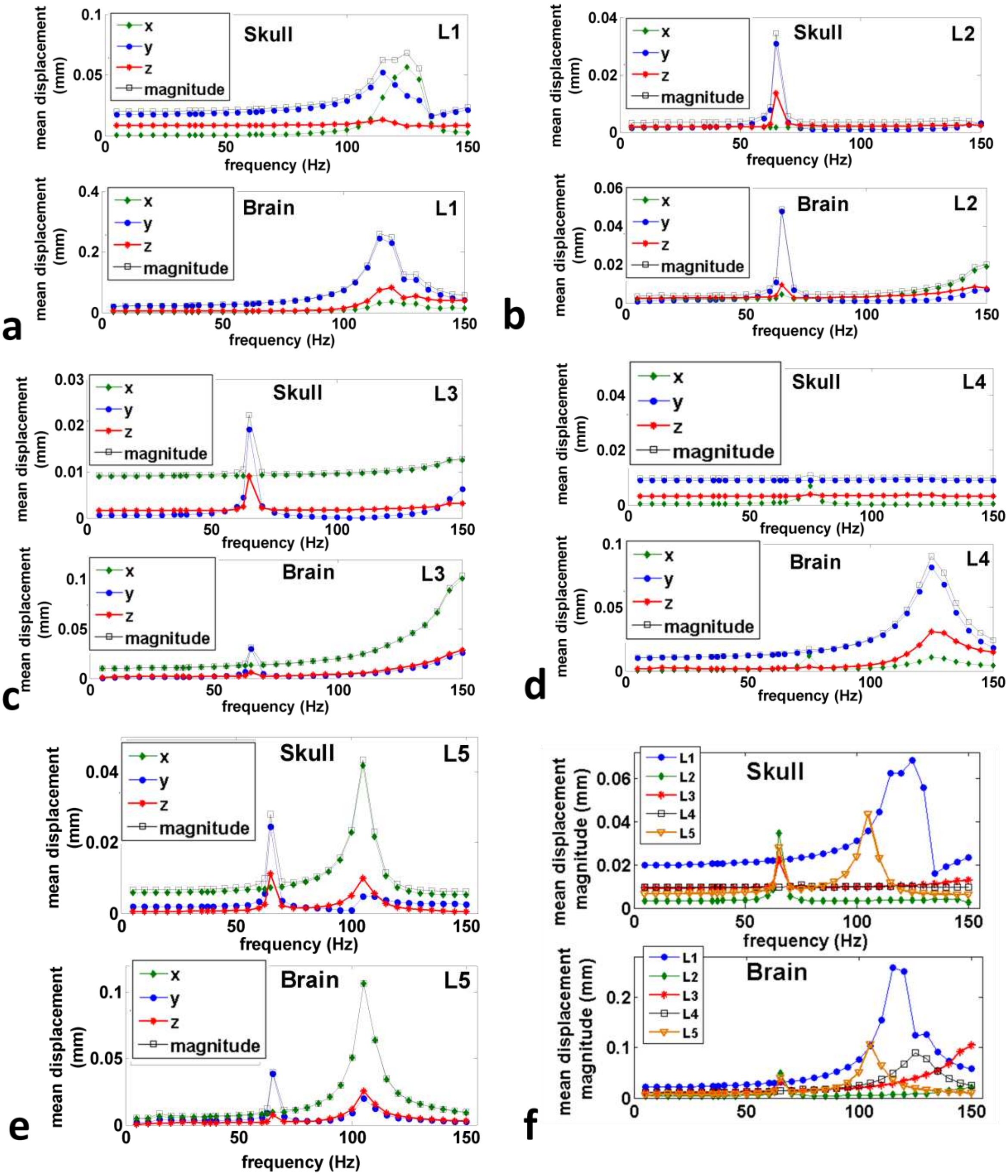

Figure 5: For XM6 model, comparison of skull and brain mean x, y and z displacement components and overall displacement magnitudes against frequency for different wave delivery methods (loading, L): a) L1; b) L2; c) L3; d) L4; e) L5; f) Comparison of mean displacement magnitudes for wave delivery methods for skull and brain.

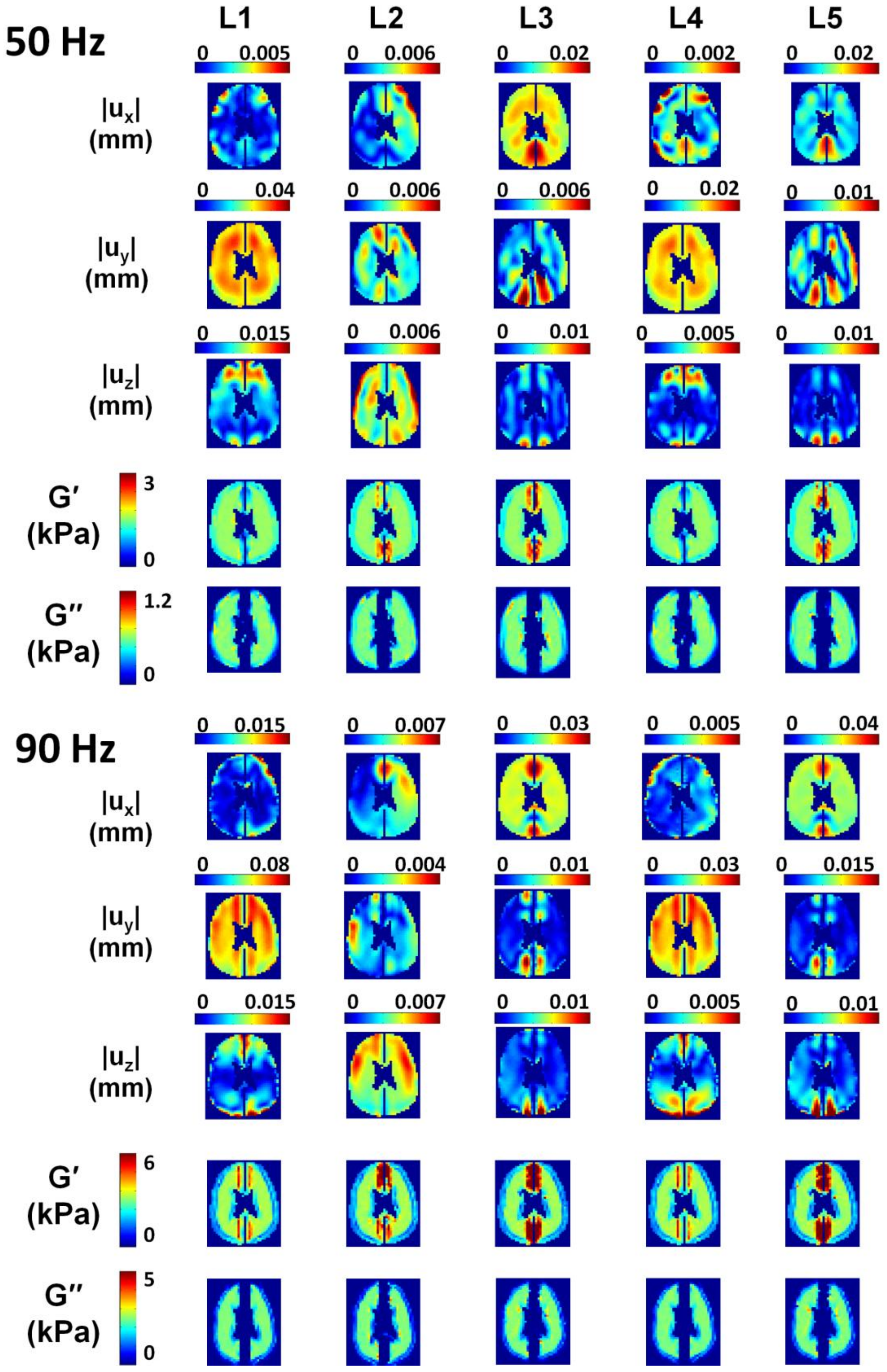

Figure 6: Comparison of displacement fields and inversion reconstructions of G' and G'' at 50 Hz and 90 Hz for different wave delivery options (loading, L).

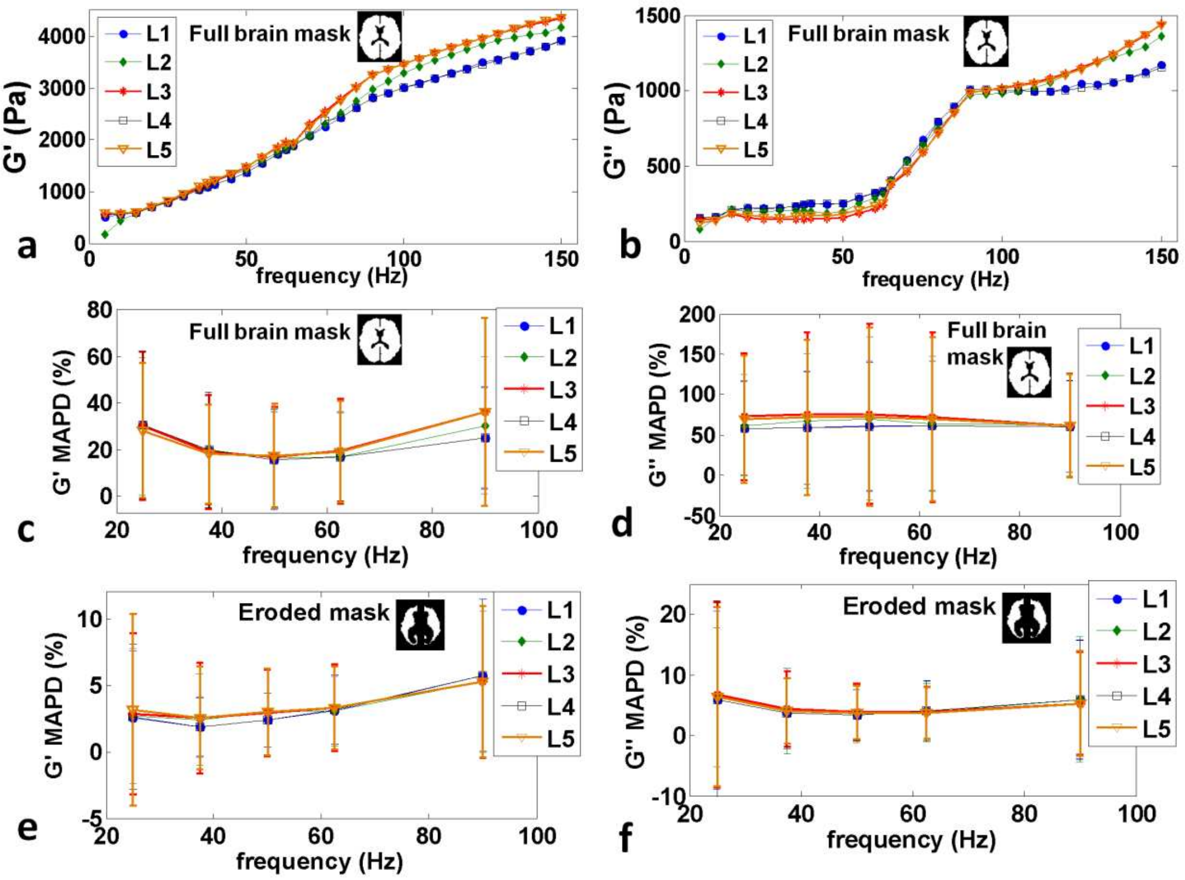

Figure 7: Comparison of mean G' and G'' from inversions of MRE simulations in XM6, and MAPD of G' and G'' for full and eroded brain masks for different wave delivery methods (loading, L). a) Mean G' for full brain mask against frequency; b) Mean G'' for full brain mask against frequency; c) MAPD of G' for full brain mask for five ground truth frequencies used in material specification for brain tissue; d) MAPD of G'' for full brain mask; e) G' MAPD for eroded brain mask; f) G'' MAPD for eroded brain mask.